Check for updates

Spatiotemporal imaging analysis of mesoscale mass transfer performance of an FCC catalyst

Lei Yu,[a] Panpeng Wei,[a] Li Zhang,[b] Yunfeng Zheng,[b] Huimin Guan,[a] Huan Wang,*[a] Yucai Qin, ![ID] *[a] Lijuan Song, ![ID] [a] Xionghou Gao*[b] and Shengwen Li[c]

The mass transfer performance of fluid catalytic cracking (FCC) catalysts is a key factor affecting the reaction activity and selectivity of catalytic cracking. This study employs confocal laser scanning microscopy with rhodamine B as a macromolecular fluorescent probe to simulate and investigate the mesoscale mass transfer behavior of heavy oil molecules on an FCC catalyst, achieving spatiotemporal imaging analysis of mass transfer patterns within catalyst microspheres. Results revealed that after 10 min, the probe molecules penetrated only about one-tenth of the microsphere's depth below the surface layer. Moreover, significant variations in concentration distribution were observed at different locations. This phenomenon stemmed from the compositional and structural heterogeneity across distinct regions of FCC catalyst particles, resulting in differential diffusion rates for the probe molecules. Combined with Fick's law calculations, the effective diffusion coefficient was determined to be in the order of 10^{-14} m^2 s^{-1}, approximately 4 orders of magnitude lower than that of the intrinsic diffusion coefficient. This result fully confirmed that the surface composition and pore structure characteristics of the catalyst impose significant diffusion limitations on the mass transfer of large molecules within the FCC catalyst microspheres. A novel visualization methodology for studying the mass transfer in FCC catalysts was successfully developed based on super-resolution fluorescence imaging technology. This approach enables the mesoscale revelation of the mass transfer mechanisms for heavy oil macromolecules within FCC catalysts, thereby offering optimization strategies for enhancing catalyst mass transfer performance.

Introduction

Fluid catalytic cracking (FCC), as an important process for the refining of heavy oil and residual oil, is a vital and central operation in a refinery. With escalating concerns over the increasing heaviness and deteriorating quality of crude oil, the development of heavy oil cracking catalysts has attracted considerable attention in the industry.[1–4] The FCC catalyst is a typically shaped material with abundant multi-dimensional, multi-scale channel structures. Improving the cracking activity of heavy oil macromolecules through enhanced mass transfer is a key strategy in developing new catalysts.[5,6] In recent years, efficient catalytic materials with superior mass transfer performance, such as hierarchical porous zeolites and macro-porous matrixes, have attracted significant attention and are increasingly applied.[7–10] However, a significant shortcoming persists in the investigation of the mass transfer performance of heavy oil macromolecules, primarily due to the absence of adequate characterization techniques capable of furnishing experimental data support.[11–13]

Currently, there are numerous ongoing debates surrounding the research findings on the mass transfer of guest molecules within the FCC catalyst particles. Barrie *et al.* explored the adsorption and desorption kinetics of model hydrocarbon molecules on the FCC catalyst particles by a taper element oscillating microbalance (TEOM). Through the alignment of a mathematical model with experimental data, it was discovered that a rapid, albeit non-rate-limiting, mass transfer occurred within the matrix. Conversely, the rate-limiting mass transfer within the FCC catalyst particles was ascribed to the molecular transfer occurring at the interface between the zeolite and the matrix.[14,15] A complex multi-scale mass transfer for *n*-octane molecules in FCC catalyst microspheres was investigated by Kärger *et al.* using pulsed field gradient nuclear magnetic resonance (PFGNMR). The diffusion that occurred in the macro-/meso-pores of the particle was the rate-limiting step under the presupposition that a rapid molecular exchange occurred between the micropores of the zeolite and the macro-/meso-porous pores of the matrix.[16]

[a]College of Petrochemical Engineering, Liaoning Petrochemical University, Fushun, 113001, Liaoning, China. E-mail: wanghuangryx@163.com; qinyucai@npu.edu.cn; lsong@lnpu.edu.com

[b]Lanzhou Petrochemical Research Center, Petrochemical Research Institute, PetroChina, Lanzhou, 730060, Gansu, China

[c]China National Aviation Fuel Group Liaoning Petroleum Co., Ltd., Shenyang, 110000, Liaoning, China

Our research group has conducted extensive work on the mass transfer properties of FCC catalysts. By employing the frequency response technique, we have achieved the discrimination of multiple kinetic processes simultaneously occurring within the hierarchical pore networks of catalyst particles. This work confirmed that the diffusion processes within the macropores/mesopores of the matrix and the molecular exchange between the matrix and zeolite pores constitute the rate-controlling steps for mass transfer inside FCC catalyst particles.[17] The above research results have preliminarily confirmed that a complex and interesting mass transfer behavior is observed in the FCC catalyst particles. However, the above-mentioned research methods still have many limitations in the study of the mass transfer law of FCC catalysts, especially the small molecular size of the selected model compounds cannot reveal the mass transfer behaviors of heavy oil macromolecules. In industrial catalysts for the catalytic conversion of heavy oils, such as *via* catalytic cracking and hydrocracking, there is a serious resistance to the diffusion of heavy oil molecules. In order to reasonably design and develop catalytic materials for the efficient conversion of heavy oils, studies on the diffusion behaviors of heavy oil molecules in catalysts under non-reactive conditions have attracted much attention.[18,19]

In recent years, fluorescence microscopic imaging technology has been widely used in the field of heterogeneous catalysis research, leading to numerous innovative achievements.[20-25] Weckhuysen *et al.*[26] employed this technology to create a distribution map of B-acid centers on a single FCC catalyst particle by selectively dyeing fluorescent active probe molecules. Kerssens *et al.*[27] applied the same method to investigate the impact of reactant molecule diffusion on the catalytic performance of the mesoporous catalyst Ti-MCM-41, visualizing the mass transfer phenomenon during the catalytic reaction process. Hendriks *et al.*[28] utilized *N,N'*-bis(2,6-dimethylphenyl)-perylene-3,4,9,10-tetracarboxylic diimide (PDI) as a molecular probe to study the single-molecule mass transfer behavior in FCC catalysts using total internal reflection fluorescence microscopy. It is evident that the unique advantage of fluorescence microscopic imaging technology lies in its ability to visualize the "time" and "space" resolutions of macromolecular probe adsorption and diffusion behaviors on porous materials. These findings significantly contributed to our understanding of the structure–activity relationship, mass transfer properties and texture properties of catalytic materials.

Addressing the critical scientific challenge of understanding how the mass transfer performance of FCC catalysts impacts their catalytic efficiency factor, this study employs laser confocal microscopy to dynamically stain and label multi-dimensional and multi-scale pores on an FCC catalyst using suitable fluorescent probe molecules. This approach enables fluorescence microscopic imaging analysis of guest molecules within catalyst particles. We developed a novel spatiotemporal imaging analysis method for studying the mesoscale mass transfer law of FCC catalysts (Fig. 1). This method offers theoretical guidance and data support for the research and development of new heavy oil catalytic cracking catalysts, providing a crucial design basis for the comprehensive upgradation of core heavy oil processing catalyst technologies.
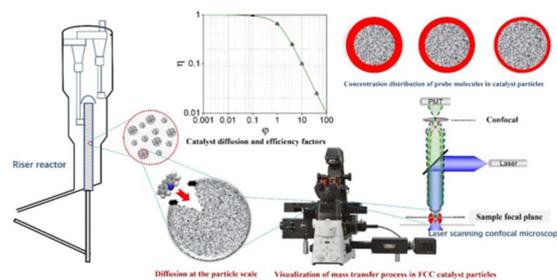

Fig. 1 Principle and schematic of spatiotemporal imaging analysis of the mesoscale mass transfer performance of FCC catalysts.

Materials and methods

Materials

FCC catalyst, Lanzhou Petrochemical Research Centre, Petrochemical Research Institute (average particle size of 100 μm). Rhodamine B ($C_{28}H_{31}ClN_2O_3$) (chromatographically pure), J&K Scientific Co., Ltd. Anhydrous ethanol (analytically pure), Sinopharm Group Chemical Reagent Co., Ltd.

Morphology and pore structure characterization of the FCC catalyst

The surface morphology of the FCC catalyst was observed using an ORION helium ion microscope (HIM, Zeiss, Germany). N_2 adsorption and desorption isotherms were measured at liquid nitrogen temperature (77 K) by an ASAP2020 automatic physical adsorption instrument of micromeritics, and the catalyst's pore structure information (specific surface area, pore volume, and pore size) was characterized.

Imaging analysis of the mass transfer law of FCC catalyst

Preparation of probe molecular solution. To prepare a 1×10^{-4} mol L^{-1} solution of rhodamine B, 0.0479 g of the dye was weighed using a 1/10 000 electronic balance, and it was dissolved in anhydrous ethanol in a 100 mL volumetric bottle. The solution was transferred to a reagent bottle, sealed, and stored for further use.

Preparation of the FCC catalyst samples. The FCC catalyst samples to be analyzed were sieved through 100–200 mesh steel screens, activated by roasting in a Muffle furnace at 773 K for 10 h, cooled to room temperature, and placed in a dryer for use.

Parameter setting of the laser confocal fluorescence microscope

A Japanese Olympus FV 1000 inverted confocal fluorescence microscope was used with a 60-times oil lens with a numerical aperture (NA) of 1.42, excitation wavelength of 543 nm, and emission wavelength of 550–650 nm.

Fluorescence imaging analysis process

1 mg of the activated FCC catalyst sample was taken and placed in a confocal special glass substrate dish. 1 mL anhydrous ethanol was added and slightly shaken to ensure that the catalyst microspheres were evenly distributed at the bottom of

the dish. Then, 10 μL of rhodamine B probe molecular solution was added dropwise. Start the timer, cover the Petri dish, and place it on the microscope stage. A catalyst microsphere with a diameter of about 100 μm and good sphericity was selected as the test object. The focal plane was adjusted to the maximum radius of the catalyst microsphere and time and space sequence tests were conducted.

Time series test. After adding the probe solution for 3 min, fluorescence images were scanned at an acquisition speed of 1 frame per second for 10 min, resulting in a total of 600 frames of images.

Spatial sequence test. After collecting the time series, the radius of the microsphere was measured to be 42 μm by moving the focal plane down along the Z-axis to the bottom of the microsphere. The Z-axis step was set to 1.4 μm per frame. The optical slice was scanned along the Z-axis of the catalyst particles, and a total of 36 frames of images were collected. This allowed for the reconstruction of three-dimensional images of the concentration distribution of probe molecules within the catalyst microsphere.

Calculation of diffusion coefficient

According to Fick's first law, in a unit of time, the flow of diffusing material through a unit cross-sectional area perpendicular to the diffusion direction (known as the diffusion flux, denoted J) is directly proportional to the concentration gradient at that cross-section. By performing a series of calculations, the quantitative effective diffusion coefficient can be determined. The fundamental mathematical representation is as follows:

$$J = -D_{eff} \times dC/dx, \tag{1}$$

In eqn (1), D_{eff} is the effective diffusion coefficient ($m^2 s^{-1}$), C is the volume concentration of the diffused substance ($mol\ m^{-3}$), dC/dx is the concentration gradient, and "−" indicates that the diffusion direction is in the opposite direction of that of the concentration gradient, that is, the diffusion component is diffused from a high concentration region to a low concentration region.

Results and discussion

Morphology and pore structure characterization of the FCC catalyst

Morphology analysis of the FCC catalyst microspheres. Fig. 2 shows the overall and local surface morphology structures of the FCC catalyst microspheres. From the SEM image in Fig. 2a, it can be seen that the selected FCC catalyst particles have good sphericity. Fig. 2b and c are images captured using a helium ion microscope. Fig. 2c shows that the specific particle diameter selected for the experiment is 100 μm. In Fig. 2b, the surface of the catalyst microspheres presents a disordered stacking state, where small particles with relatively regular shapes are the molecular sieve crystal clusters that are randomly combined with the amorphous matrix material through binders. This is consistent with the morphological characteristics of the FCC catalyst particles obtained through the traditional spray drying process.[29]
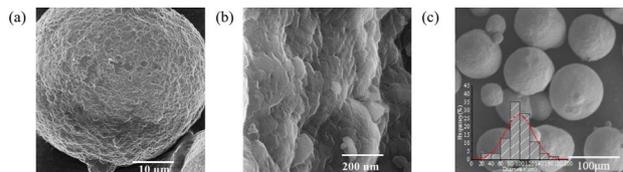

Fig. 2 Surface morphology images of the FCC catalyst microspheres.

According to previous studies,[30] within an FCC catalyst microsphere, the molecular sieve, substrate, and other auxiliary components are primarily in a random distribution, resulting in a robust disordered pore structure. Notably, the molecular sieve serves as the primary active component of the FCC catalyst and is randomly distributed throughout the microspheres. Consequently, accessibility of the active components of the molecular sieve to heavy oil macromolecules has become a critical factor in determining the cracking activity of the catalyst. This accessibility heavily relies on the mass transfer performance of heavy oil macromolecules on the catalyst surface.

Pore structure analysis of the FCC catalyst microspheres

Fig. 3 displays the N_2 adsorption–desorption isotherm and pore size distribution curve of the FCC catalyst. By referencing the 2015 report of the International Union of Pure and Applied Chemistry (IUPAC) for the classification and definition of isotherm and hysteresis loops, it is evident that the adsorption branch of the adsorption–desorption isotherm consists of type I and type II isotherms, while the hysteresis loop falls under type H4. This is the typical curve of a solid material with narrow fissure pores, and it can be obtained from the data in Table 1 that the sample has abundant microporous structures. This is due to the gap pore structure formed by the aggregation of zeolite molecular sieve crystals and matrix materials in the FCC catalyst microspheres.[31]

Time-resolved imaging analysis of the macromolecule mass transfer in the FCC catalyst

By focusing on the plane close to the center of a single FCC catalyst microsphere, we can capture the dynamic mass transfer process of probe molecules from the surface to the interior of the microsphere over time. Fig. 4 showcases four snapshots at different time points during the imaging process. The initial frame, captured 3 min after the introduction of the probe molecule, highlights the stained area (red) at the edge of the
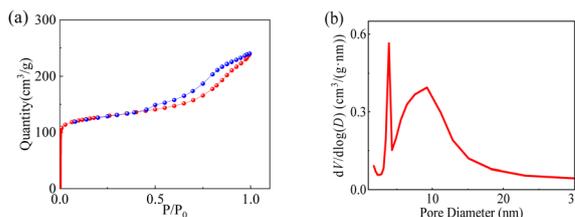

Fig. 3 Textural properties of the FCC catalyst: (a) N_2 adsorption–desorption isotherm; (b) desorption $dV/d\log(D)$ pore volume.

Table 1 Parameters of textural properties of the catalyst sample

Micropore area (m^2 g^{-1})	Mesoporous area (m^2 g^{-1})	Micropore volume (cm^3 g^{-1})	Mesoporous volume (cm^3 g^{-1})
276	118	0.144	0.227

catalyst microsphere. Notably, dyeing depths vary across different regions. Subsequent frames (2 to 4) taken at the 6th, 9th, and 12th min, respectively, illustrate how the dyeing depth progressively increases over time, which is especially evident at the right edge of the microsphere within the field of view. Additionally, the red region at the microsphere's center also expands with time. These observations demonstrate that laser confocal fluorescence microscopy can be effectively used to visualize the internal molecular mass transfer process of fluorescent probes within molded catalyst particles.

Through the quantitative analysis of fluorescence brightness across different regions and time points, we quantitatively assessed the variations in fluorescence intensity (which is directly related to probe molecule concentration) on FCC catalyst microspheres over time. Results (presented in Fig. 5) reveal distinct patterns across the four selected regions (1–4 in Fig. 5a). A closer examination of the fluorescence intensity distribution within each region (Fig. 5b) reveals significant differences in fluorescence intensity across all the regions. Fig. 5c presents the temporal evolution of the average fluorescence intensity in these four regions on the catalyst. Notably, there is a strong linear positive correlation between the average fluorescence intensity and adsorption time, indicating that rhodamine B molecules gradually diffuse into the catalyst particles, resulting in a growing number of chromophore molecules on the catalyst particles. Furthermore, it is evident that the initial concentration of rhodamine B molecules and the slope of the adsorption rate curve vary across different regions of the catalyst particles, indicating that the diffusion rate of rhodamine B molecules differs in various regions due to variations in the FCC catalyst's composition and pore structure.
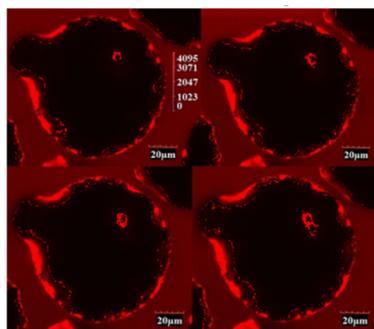
Notably, abrupt changes occur in the initial and steady-state rates across different regions (Table 2) because (i) regions 1–2 contain more surface macropores, resulting in faster initial adsorption rates but forming deeper diffusion barriers and (ii) regions 3–4 exhibit higher zeolite micro-cluster density, demonstrating rapid initial adsorption while achieving sustained diffusion through interconnected mesopores. Investigation of saturation effects reveals that while surface sites in regions 1–2 approach saturation, bulk diffusion continues in regions 3–4.

Imaging analysis of the three-dimensional distribution characteristics of probe molecules on the FCC catalyst microspheres

After the catalyst is sufficiently impregnated with a 10^{-4} mol L^{-1} rhodamine B probe solution and filling its pores with probe molecules, laser scanning confocal microscopy is conducted. Utilizing a high-precision stepper motor to drive the FCC catalyst microsphere sample along the Z-axis enables optical sectioning. Subsequent software processing then reconstructs a 3D image, visualizing the distribution characteristics of probe molecules on the FCC catalyst microsphere. Fig. 6 presents an optical slice tomography image of the distribution of rhodamine B molecules on a single FCC catalyst particle. By analyzing the fluorescence distribution across different Z-axis sections of the catalyst particle after 13 min of rhodamine B adsorption, it is evident that rhodamine B molecules are primarily concentrated within a specific thickness range (approximately 5 μm) at the surface layer of the catalyst particle. Additionally, the optical slice clearly reveals the presence of a void defect within the FCC catalyst particle, which is connected to the external environment. This structural feature facilitates the rapid diffusion of
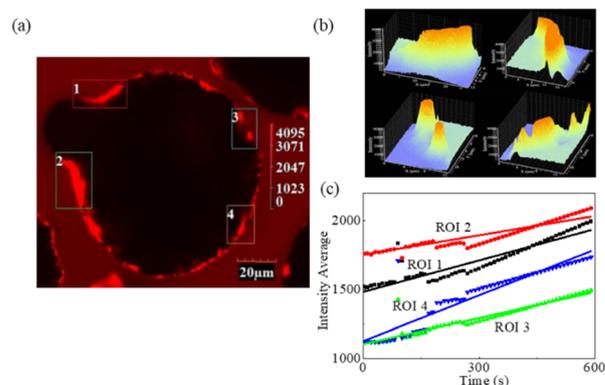

Fig. 4 Time-resolved imaging of the diffusion of rhodamine B into a catalyst particle (60× oil objective lens, NA: 1.42): The first picture shows the state the 3th minute after adding the probe molecule solution, the second picture shows it at the 6th minute, the third picture at the 9th minute, and the fourth picture again at the 12th minute; $\lambda_{ex} = 543$ nm, $\lambda_{em} = 550–650$ nm.

Fig. 5 Changes in the fluorescence distribution catalyst particles upon the adsorption of rhodamine B at 10^{-4} mol L^{-1} with time: (a) different regions of the catalyst particles; (b) fluorescence intensity of each pixel in the corresponding region of the catalyst particle after adsorbing rhodamine B; and (c) average fluorescence intensity variations in regions 1–4 with time.

Table 2 Calculated initial adsorption rates and steady-state diffusion rates for the four regions

Region	Initial rate (min^{-1})	Steady state (min^{-1})
1	2.4	1.8
2	2.1	1.6
3	1.7	2.0
4	1.5	2.2

macromolecules into the catalyst microsphere, confirming that a through-macropore structure is an optimal configuration for enhancing the mass transfer and accessibility of heavy oil macromolecules in FCC catalysts. Fig. 7 displays the 3D reconstructed fluorescence image of a single FCC catalyst particle following rhodamine B adsorption. Notably, the fluorescence intensity generated by rhodamine B adsorption and enrichment varies significantly across different regions of the catalyst particle surface, indicating the distinct surface compositions and pore structures of the FCC catalyst.

Quantitative analysis of the mass transfer behavior of macromolecules in the FCC catalyst particles

The diffusion coefficient is a key physical quantity that characterizes the rate of diffusion of a substance within a porous medium. It is denoted by D and has the unit of m^2 s^{-1}, and it represents the amount of material that passes through a specific area in a given period of time. The precise calculation of the diffusion coefficient can be performed through theoretical models or experimental methods.

Stokes–Einstein equation to calculate the intrinsic diffusion coefficient

The Stokes–Einstein equation is an equation that describes the relationship between viscosity and diffusion coefficient. It offers a means for calculating the molecular diffusion coefficient of a solute in a solution, which is influenced by various factors such as molecular size, system temperature, and solvent viscosity.[32] The equation is as follows:

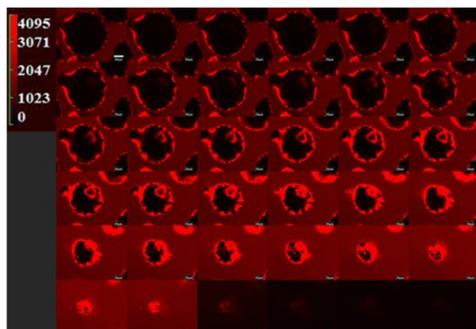$$D_{\mathrm{b}} = kT/(3\eta\pi \mathrm{d}r) \tag{2}$$

Fig. 6 Z-Scan of a single FCC catalyst particle after the adsorption of rhodamine B; Z axis stepper: 1.4 μm per frame.
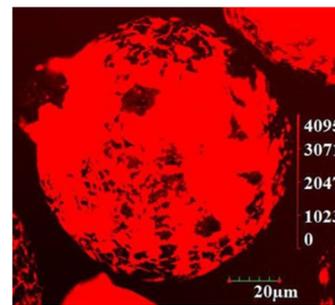

Fig. 7 3D reconstruction picture of a single FCC catalyst particle with adsorbed rhodamine B.

where k is the Boltzmann constant, 1.38×10^{-23} J K^{-1}; T is the system temperature in Kelvin; η is the viscosity of anhydrous ethanol, 0.0011 Pa s; and dr is the molecular size of rhodamine B, 1.59 nm.

Based on the Stokes–Einstein equation, the intrinsic diffusion coefficient (D_{b}) of rhodamine B in anhydrous ethanol was calculated to be 1×10^{-9} m^2 s^{-1}. However, the effective diffusion coefficient (D_{eff}) of guest molecules on porous catalysts is influenced not only by the ratio of diffused molecular diameter to catalyst pore diameter λ but also by the curvature factor of the catalyst pore structure. When the pore sizes of the guest molecule and the catalyst are similar, it falls under configurational diffusion, leading to an increase in the interaction between the pore wall and guest molecule, thereby reducing the effective diffusion coefficient of the diffused molecule. The effective diffusion coefficient of heavy oil macromolecules in the catalyst can be calculated using eqn (3):

$$D_{\mathrm{eff}} = \frac{\varepsilon}{\tau} \times D_{\mathrm{b}} \times F(\lambda), \tag{3}$$

where D_{eff} is the effective diffusion coefficient, m^2 s^{-1}; D_{b} is the intrinsic phase diffusion coefficient, m^2 s^{-1}; ε is the catalyst porosity; τ is the catalyst micropore diffusion factor, and $F(\lambda)$ is the diffusion retardation factor, $F(\lambda) = 1$–0.52λ, where λ is the ratio of molecular diameter to catalyst pore size.

Based on the literature,[33,34] an FCC catalyst with τ in the range 2–7 is recommended. For this study, $\tau = 5$ has been chosen. Consequently, the effective diffusion coefficient D_{eff} of rhodamine B molecule in the FCC catalyst channel is calculated to be 3.7×10^{-10} m^2 s^{-1}.

Diffusion coefficient calculated from the diffusion flux according to Fick's first law

In light of the above results, in combination with the principle of calculating diffusion coefficient through diffusion flux using Fick's first law (eqn (1)), it is evident that the time-resolved fluorescence imaging data of macromolecules' mass transfer process in the FCC catalyst, obtained *via* laser confocal microscopy, is well-suited for quantitative analysis of the diffusion coefficient. This work has successfully derived a reasonable effective diffusion coefficient by meticulously controlling the experimental conditions such as amount of the catalyst, concentration and volume of the solvent, and diffusion time (Fig. 8).

Based on the staining depth at the spherical cross-section of the FCC catalyst after the adsorption of rhodamine B molecules for 13 min, the estimated average depth of probe molecules diffusing into the catalyst is 5 μm, is estimated ($dx = 5$ μm), as shown in Fig. 8. To simplify calculations, it is assumed that the average catalyst particle size used in this experiment is 100 μm, and the true density of catalyst particles is treated at 1 g cm^{-3}. The total number of 0.1 mg catalyst samples is about 200. Furthermore, it is assumed that 1×10^{-10} mol rhodamine B molecules in the added 1 μL solution are uniformly adsorbed by the catalyst, which means that 5×10^{-13} mol rhodamine B molecules are adsorbed by each catalyst within 13 min. The overall adsorption rate of each catalyst is calculated as $r_{total} = 6.4 \times 10^{-16}$ mol s^{-1}. Assuming that all rhodamine B molecules uniformly diffused from the surface of the catalyst microsphere to the catalyst particles, the diffusion flux $J = 2 \times 10^{-8}$ mol·(m^2 s)$^{-1}$ is obtained. Assuming that rhodamine B molecules are uniformly adsorbed in the outer layer of the catalyst with a thickness of 5 μm, the concentration of adsorbed molecules on the catalyst is obtained as 3.6 mol m^{-3}, that is, $dC = 3.6$ mol m^{-3}.

Using the data provided, along with Fick's first law (eqn (1)), the diffusion coefficient of rhodamine B molecules in the FCC catalyst particles is calculated as 2.8×10^{-14} m^2 s^{-1}. When compared with the results obtained through the theoretical model, it becomes evident that the effective diffusion coefficient obtained through the theoretical model is approximately four orders of magnitude higher than that of the experimental measurement. This significant difference can be attributed to the intricate molecular diffusion behavior within the FCC catalyst particles, which is more complex than what is captured by the theoretical model. This complexity involves factors such as limitations to the degree of molecular diffusion, diameter and properties of the diffusion molecules, and the close correlation with catalyst pore structure and other properties.[35]

Diffusion coefficient calculated from the adsorption rate according to Fick's second law

Based on the curves of the average fluorescence intensity at four different regions on the FCC catalyst in Fig. 5c, and considering that the fluorescence intensity on the FCC catalyst microspheres is positively correlated with the molecular weight of the local adsorbed probe molecules, the quantitative analysis of the local diffusion coefficient can be achieved using the Fick's second law formula (4).[17]
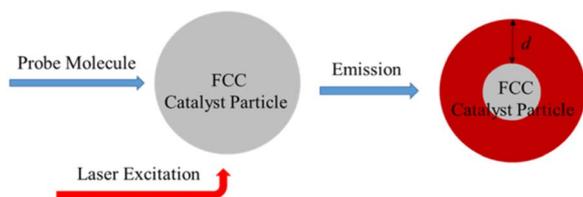

Fig. 8 Schematic of the calculation of diffusion coefficients in different stages of a single FCC catalyst particle.

$$\frac{I_t - I_0}{I_\infty - I_0} = \frac{I_t}{I_\infty} = 1 - \frac{6}{\pi^2} \sum_{n=1}^{\infty} \left[\frac{1}{n^2} \exp\left(-\frac{n^2 \pi^2 t}{r_0^2} D \right) \right], \quad (4)$$

$$\frac{I_t - I_0}{I_\infty - I_0} = \frac{I_t}{I_\infty} \approx \frac{6}{\sqrt{\pi}} \left(\frac{Dt}{r_0^2} \right)^{1/2}, \quad (5)$$

In these equations, I_0, I_t, and I_∞ are the average fluorescence intensity at the beginning of the data recording (when the solution is added for 3 min), time t, and the end point of the adsorption (when the solution is added for 13 min), respectively. Given the highly linear relationship between fluorescence intensity and adsorption time in Fig. 5c, eqn (4) can be simplified to eqn (5). The diffusion coefficients of rhodamine B on the FCC catalyst particles were 1.62×10^{-14} m^2 s^{-1}, 1.26×10^{-14} m^2 s^{-1}, 1.67×10^{-14} m^2 s^{-1}, and 4.53×10^{-14} m^2 s^{-1}, respectively. It is observed that the diffusion coefficients obtained through Fick's second law and Fick's first law are approximately one order of magnitude lower than the values calculated using the theoretical model. Furthermore, the diffusivity values of the four selected regions differ, which can be attributed to variations in the pore structure leading to distinct diffusion limitations for guest molecules.[36,37]

Conclusion

This study employed confocal laser scanning microscopy with rhodamine B as a fluorescent probe to investigate the mesoscale mass transfer behavior of heavy oil molecules in an FCC catalyst. Results demonstrated significant heterogeneity in the adsorption and diffusion rates across different regions of the catalyst particles, with probe molecules penetrating only about one-tenth of the microsphere's depth after 10 min. The effective diffusion coefficient, calculated using Fick's law, was found to be in the order of 10^{-14} m^2 s^{-1}, approximately 3–4 orders of magnitude lower than that of the intrinsic diffusion coefficient derived from the Stokes–Einstein equation. This discrepancy highlighted the complexity of molecular diffusion within the catalyst, which is influenced by both the properties of the diffusing molecules and the pore structure of the catalyst.

The spatiotemporal imaging analysis method developed here provides a novel approach for visualizing and quantifying mass transfer processes in FCC catalysts at the mesoscale. This methodology not only advances our understanding of mass transfer mechanisms but also offers valuable insights for optimizing catalyst design to improve heavy oil conversion efficiency. The findings underscore the importance of pore structure and compositional homogeneity in enhancing the catalyst performance, paving the way for future research and developments in this field.

Author contributions

Lei Yu: writing-original draft. Panpeng Wei: formal analysis. Li Zhang: supervision. Yunfeng Zheng: formal analysis. Huimin Guan: validation. Huan Wang: writing-review and editing. Yucai Qin: project administration. Lijuan Song: methodology. Xionghou Gao: conceptualization. Shengwen Li: formal analysis.

Conflicts of interest

There are no conflicts to declare.

Data availability

The data that support the findings of this study are available from the corresponding author upon reasonable request.

Acknowledgements

Notes and references

1 E. N. Al-Shafei, A. N. Aljishi, Z. M. Shakoor, M. Z. Albahar, M. F. Aljishi and A. AlasseelL, *RSC Adv.*, 2023, **13**, 25804–25810.

2 D. E. Adanenche, A. Aliyu, A. Y. Atta and B. J. El-Yakubu, *Fuel*, 2023, **343**, 127894.

3 M. S. Marschall, M. Seifert, M. Hauck, O. Busse and J. J. Weigand, *Mater. Today Commun.*, 2024, **41**, 110234.

4 Z. Yanliang, X. Lu, W. Zhang, H. Chen, G. Li, J. Zhang, Z. Li and J. Wang, *Russ. J. Phys. Chem. A*, 2024, **98**, 1740–1751.

5 Q. I. Yan-ping, C. Sheng-li, D. Peng, X. U. Ke-qi and S. Bao-jian, *J. Fuel Chem. Technol.*, 2006, **34**, 685–690.

6 E. N. Shafei, A. Masudi, Z. H. Yamani and O. M. K. Tovbin, *RSC Adv.*, 2022, **12**, 18274–18281.

7 M. H. Sun, L. H. Chen, S. Yu, Y. Li, X. G. Zhou, Z. Y. Hu, Y. H. Sun, Y. Xu and B. L. Su, *Angew. Chem., Int. Ed.*, 2020, **59**, 19582–19591.

8 M. Pan, J. Zheng, Y. Liu, W. Ning, H. Tian and R. Li, *J. Catal.*, 2019, **369**, 72–85.

9 W. Cui, D. Zhu, J. Tan, N. Chen, D. Fan, J. Wang, J. Han, L. Wang, P. Tian and Z. Liu, *Chin. J. Catal.*, 2022, **43**, 1945–1954.

10 M. Abdi-Khanghah, A. Jafari, G. Ahmadi and A. Hemmati-Sarapardeh, *Energy*, 2023, **284**, 128267.

11 Y. Y. Petrova, E. V. Frantsina, A. A. Grin'ko, A. Y. Pak, V. V. Arkachenkova and P. V. Povalyaev, *Mater. Today Commun.*, 2022, **33**, 104669.

12 H. Wang, J. Zhang, L. Song and Y. Qin, *J. Petrochem. Univ.*, 2021, **34**, 1–8.

13 V. V. Zhivonitko, Z. Vajglová, P. Mäki-Arvela, N. Kumar, M. Peurla and D. Y. Murzin, *Russ. J. Phys. Chem. A*, 2021, **95**, 547–557.

14 E. Alpay, D. Chadwick, L. S. Kershenbaum, P. J. Barrie, C. Sivadinarayana and L. F. Gladden, *Chem. Eng. Sci.*, 2003, **58**, 2777–2784.

15 C. K. Lee, S. Ashtekar, L. F. Gladden and P. J. Barrie, *Chem. Eng. Sci.*, 2004, **59**, 1131–1138.

16 P. Kortunov, S. Vasenkov, J. Kärger, M. Fé Elía, M. Perez, M. Stöcker, G. K. Papadopoulos, D. Theodorou, B. Drescher, G. McElhiney, B. Bernauer, V. Krystl, M. Kocirik, A. Zikanova, H. Jirglova, C. Berger, R. Gläser, J. Weitkamp and E. W. Hansen, *Magn. Reson. Imaging*, 2005, **23**, 233–237.

17 Y. Qin, X. Gao, H. Zhang, S. Zhang, L. Zheng, Q. Li, Z. Mo, L. Duan, X. Zhang and L. Song, *Catal. Today*, 2015, **245**, 147–154.

18 S. A. Bonke, T. Risse, A. Schnegg and A. Brückner, *Nat. Rev. Methods Primers*, 2021, **1**, 33.

19 W. Wang, *Nat. Chem.*, 2019, **11**, 17–18.

20 J. J. E. Maris, Y. Ganjkhanlou, C. Versluis, R. Mayorga González, N. Nikolopoulos, F. T. Rabouw, E. T. C. Vogt, B. M. Weckhuysen and F. Meirer, *ACS Cent. Sci.*, 2025, 872–877.

21 R. Vogel, C. Versluis, R. Frijsen, P. T. Prins, E. T. C. Vogt, F. T. Rabouw and B. M. Weckhuysen, *Angew. Chem., Int. Ed.*, 2024, **63**, e202409503.

22 Y. Xiao and W. Xu, *Chem*, 2023, **9**, 16–28.

23 R. M. González, J. J. E. Maris, M. Wagner, Y. Ganjkhanlou, J. G. Bomer, M. J. Werny, F. T. Rabouw, B. M. Weckhuysen, M. Odijk and F. Meirer, *Angew. Chem., Int. Ed.*, 2024, **63**, e202314528.

24 M. J. Werny, K. B. Siebers, N. H. Friederichs, C. Hendriksen, F. Meirer and B. M. Weckhuysen, *J. Am. Chem. Soc.*, 2022, **144**, 21287–21294.

25 P. A. López and S. A. Blum, *ACS Catal.*, 2024, **14**, 17132–17147.

26 E. C. Nordvang, E. Borodina, J. Ruiz-Martínez, R. Fehrmann and B. M. Weckhuysen, *Chem.–Eur. J.*, 2015, **21**, 17324–17335.

27 M. M. Kerssens, C. Sprung, G. T. Whiting and B. M. Weckhuysen, *Microporous Mesoporous Mater.*, 2014, **189**, 136–143.

28 F. C. Hendriks, F. Meirer, A. V. Kubarev, Z. Ristanović, M. B. J. Roeffaers, E. T. C. Vogt, P. C. A. Bruijnincx and B. M. Weckhuysen, *J. Am. Chem. Soc.*, 2017, **139**, 13632–13635.

29 X. P. Yin, Y. Li, H. Fan and B. K. Jiang, *Acta Pet. Sin.*, 2023, **39**, 109–119.

30 Z. Y. Liu, Y. F. Wang, B. Y. Wu, T. Liu and X. H. Gao, *Pet. Refin. Eng.*, 2023, **53**, 65–68.

31 R. Q. Lv, J. Gu, B. Tang and S. H. Xiang, *J. Fuel Chem. Technol.*, 2004, **32**, 504–509.

32 W. M. Deen, *AlChE J.*, 1987, **33**, 1409–1425.

33 R. E. Baltus, *Fuel Sci. Technol. Int.*, 1993, **11**, 783–830.

34 Z. G. Wang, J. N. Pei, S. L. Chen, Q. Cai and Y. F. Lou, *J. Chem. Eng. Chin. Univ.*, 2014, **28**, 8.

35 Z. Y. Liu, S. L. Chen, P. Dong, X. J. Ge and Y. D. Sun, *J. Petrochem. Univ.*, 2011, **24**, 1–5.

36 A. Ghosh, H. Pham, J. Higgins, F. V. Swol, A. DelaRiva, M. Melton, D. Kunwar, G. S. Qi, S. H. Oh, M. Wiebenga, W. Li and A. K. Datye, *Appl. Catal., A*, 2020, **607**, 117858.

37 M. T. Bore, T. L. Ward, A. Fukuoka and A. K. Datye, *Catal. Lett.*, 2004, **98**, 167–172.